



Dry powders reflectance model based on enhanced backscattering: case of hematite α -Fe₂O₃

Morgane Gerardin, Pauline Martinetto, Nicolas Holzschuch

► To cite this version:

Morgane Gerardin, Pauline Martinetto, Nicolas Holzschuch. Dry powders reflectance model based on enhanced backscattering: case of hematite α -Fe₂O₃. Journal of the Optical Society of America. A Optics, Image Science, and Vision, 2023, 40 (9), pp.1817-1830. 10.1364/JOSAA.487498 . hal-04316639v1

HAL Id: hal-04316639

<https://inria.hal.science/hal-04316639v1>

Submitted on 30 Nov 2023 (v1), last revised 1 Dec 2023 (v2)

HAL is a multi-disciplinary open access archive for the deposit and dissemination of scientific research documents, whether they are published or not. The documents may come from teaching and research institutions in France or abroad, or from public or private research centers.

L'archive ouverte pluridisciplinaire **HAL**, est destinée au dépôt et à la diffusion de documents scientifiques de niveau recherche, publiés ou non, émanant des établissements d'enseignement et de recherche français ou étrangers, des laboratoires publics ou privés.



Distributed under a Creative Commons Attribution 4.0 International License

Dry powders reflectance model based on enhanced back-scattering: case of hematite $\alpha - \text{Fe}_2\text{O}_3$

MORGANE GERARDIN,^{1,2,*} PAULINE MARTINETTO,² AND NICOLAS HOLZSCHUCH¹

¹Univ. Grenoble Alpes, CNRS, Inria, Grenoble INP, LJK, 38000 Grenoble, France

²Univ. Grenoble Alpes, CNRS, Institut Néel, 38000 Grenoble, France

*gerardin.morgane@gmail.com

Abstract: By performing Bidirectional Reflectance Distribution Function (BRDF) measurements, we have identified back-scattering as the main phenomena involved in the appearance of dry nano-crystallized powders. We have developed an analytical and physically based BRDF model which relies on the enhanced back-scattering theory to accurately reproduce the measurements performed on optically thick layer of dry powders with various grains' morphology. Our results are significantly better than the ones obtained with previously existing models. The model has been validated against the BRDF measurements of multiple synthesized nano-crystallized and mono-disperse $\alpha - \text{Fe}_2\text{O}_3$ hematite powders. We also discuss the ability of our model to be extended to other material or more complex powder morphology.

© 2023 Optica Publishing Group

1. Introduction

Accurate reproduction of powdered material appearance is an important issue in many domains such as environmental sciences, teledetection, digital prototyping, entertainment and art preservation. Powder materials are ubiquitous in real life, either used with a binder like pigments in most painting techniques and in some cosmetics such as lipstick, or dry such as spices, dry soils, dust, and pigments. The latter are particularly important as they are involved in parietal paintings from paleolithic to neolithic era. Some of them have been subject to many degradations processes to the point of becoming almost illegible. The digital reproduction of such cultural heritage artifacts through photo-realistic images synthesis will be of great interest for their preservation and will promote their broadcasting to a large audience.

Their appearance and more specifically the color of a powder material depends on both its chemical composition and on its morphometry, which refers to the size and the shape of its grains. This hypothesis is well known and particularly well justified in the case of pure $\alpha - \text{Fe}_2\text{O}_3$ hematite powders that can show various shades going from light red to purple [1,2]. The chemical composition of the material is involved in the absorption phenomena, while the morphology of the grains influences the way light is scattered by the material. Such light/matter interactions at the nanometric scale result in the macroscopic material appearance an observer perceive.

The light scattering by a material is numerically described using a *Bidirectional Scattering Distribution Function* (BSDF) model. Most of them assume that the light is mainly scattered at the surface of an object, around the specular direction that is to say in the direction opposite to the incident direction. Depending on the roughness of the surface, a more or less diffuse look is obtained. These models are not suitable in the case of dry powders for two reasons. First, powders are a medium composed of a collection of randomly oriented scatterers, so light is scattered multiple times in the volume of the medium, which is not taken into account by the surface models. To overcome this issue, one may use the Mie scattering theory [3]. This is relevant for powders diluted into a binder, and takes into account volume scattering depending on

the size and shape of the grains. But in the absence of a binder the grains composing the powder are too close to each other to actually be modeled using such model [2]. The second issue is that surface scattering models do not account for any scattering in the backward direction.

In this paper, we show that contrary to the prediction of most BSDF models the major contribution to a dry powder BSDF is not the specular peak but the back-scattering peak. We propose an analytical and physically-based BSDF model involving six parameters able to simulate the appearance of optically thick layer of dried pigments. We separate the model into two independent contributions: volume scattering and surface scattering. The former decomposes into single scattering and multiple scattering responsible for the sharp back-scattering lobe while the latter accounts for the specular scattering. This model has been developed and experimentally validated for seven hematite $\alpha - \text{Fe}_2\text{O}_3$ powders of different morphology. Our model reproduces the color variations of the studied samples, and can be applied to other pigments.

In Section 2 we will review previous works on BSDF models suitable for the description of dry powder materials, and more particularly on models that take into account the back-scattering contribution. The theoretical background necessary for the modeling of light scattering in a particle medium is introduced in Section 3. The $\alpha - \text{Fe}_2\text{O}_3$ samples and their measurements are described in Section 4. The description of our appearance model is done on Section 5 while in Section 6 we present its results, showing that it fits well the experimental BRDF of the studied samples. We conclude and give some future work directions in Section 7.

2. Previous work

Most of the BSDF models that are used in physically based renderers assume that the light is mainly scattered at the surface of an object, and in the specular direction which is to say the direction opposite to the incident direction. According to these models, the color of the rendered materials only depends on their chemical composition through the optical constants. In the case of participating media, the appearance also depends on physical properties and more particularly on the morphology of the involved scatterers. For diluted media, this is well described by the Lorenz-Mie scattering theory [3,4].

Dry powders and pigments are even complex materials composed of a quite dense collection of particles with nanometric to micrometric grains' size. In the absence of a binder, the dry grains are too close to each other to be modeled using Mie scattering theory [2]. Their appearance is the result of absorption and scattering phenomena, so its description suggests the full understanding of the interactions of light with the material at both its surface and in its volume.

The incoming light is partially scattered at the surface of the material. This phenomenon can be empirically modeled using the microfacet model [5] by considering that the surface is made of small but larger than wavelength specular micro facets with known orientations distribution. Alternatively, the generalized Harvey-Shack theory [6] allows to predict the reflectance of a rough surface while taking into account the diffraction effects caused by surface asperities. It accurately simulates the appearance of opaque and homogeneous materials but only considers single scattering.

As we will show in this paper, in the case of pigments an important amount of the incoming light is scattered backwards, responsible for a high peak back into the incident direction. This scattering phenomena, known as *back-scattering*, has already be observed on other dry powders such as meteorites soils [7], and has already been taken into account in some BRDF models: the spectralon model, the RTLSR model and the enhanced back-scattering model.

2.1. Spectralon

An empirical one has been developed by [8] to model the BRDF of the Spectralon®, a material that resembles a powder since it is made out of a collection of compressed polymer particles.

This model is assumed to be the summation of four independent scattering phenomena, occurring at both the surface and in the volume of the material. As it involves a large number of material-dependent parameters optimized in the specific case of Spectralon, it can be adapted to reproduce with a high fidelity a large range of materials. Nevertheless, these parameters has no explicit relationship with the chemical composition nor the physical parameters of the considered material so they cannot be predicted, but only deduced from measurement fittings.

2.2. RTLSR

The RTLSR (Ross-Thick Li-Sparse Reflectance) model [9, 10], is a semi-empirical model used in teledetection for simulating the BRDF of forest canopies. It decomposes the BRDF into a volume scattering contribution deduced from an approximation of the radiative transfer theory (RT) [11], and surface scattering which is inferred according to purely geometrical considerations [12]. An optimization factor allows to control the proportion of each of the contributions. Initially developed for thick and sparse canopies, extensions of this model have been proposed for thin and dense media [13]. [14] brought modifications to the model for the study of snow, and multiple works [12, 15, 16] agree that it can be used for bare soils although they do not explicitly introduce the changes that should be done in such a case. Because of its unique controllable parameter, this model is too rigid and remains unable to reproduce fine appearance variations.

2.3. Enhanced Back-scattering

A deeper analysis of the back-scattering phenomena (see Section 3.5) occurring in a scattering medium refers to *Enhanced Back-Scattering (EBS)*, which describes it as the result of constructive interferences [17], [18]. Contrary to the RT theory, the scattered fields are supposed to be correlated. As a result, the EBS is the sum of the two terms of RT theory (*single* and *multiple scattering*) and a third one accounting for the constructive interferences in the backward direction. As the analytical results are deduced within the diffusion approximation, only isotropic particles are considered. Nevertheless, [17] extended the model to account for anisotropic scattering in the case of normal incidence.

3. Background

As a dry powder layer involves a large number of scatterers with relatively high density, it is complex to describe the scattering of light in such a medium. Most of the time, it can be done using the radiative transfer theory (RT) [19], [20], which accounts for both single and multiple scattering inside the medium. As it relies on the assumption that the scattered fields are uncorrelated, RT is unable to predict the appearance of materials which exhibits a strong back-scattering contribution. In this section, let's overview the theoretical aspects and hypotheses useful for an extension of RT known as the enhanced back scattering theory (EBS), that takes into account correlated scattered fields to describe the back-scattering phenomenon.

3.1. Medium description

Let's consider a region 0 free of scatterers with wavenumber $k_0 = 2\pi/\lambda$, and a medium 1 characterized by an effective wavenumber $K = K' + iK''$ containing N scattering spherical inclusions per unit volume. All scatterers have the same radius r and scattering properties (Figure 1).

The medium is illuminated in the incoming direction θ_i by the light coming from a point source at the position \mathbf{r}_i in the region 0. The light scattered by the slab is observed at a point in region 0 in the direction (θ_o, φ) at a distance $r_o \gg 1$ from the interface. To ease the description of the scattering inside the layer, point scatterer approximation is made: the scattering events occur at the center point of the spherical scatterers.

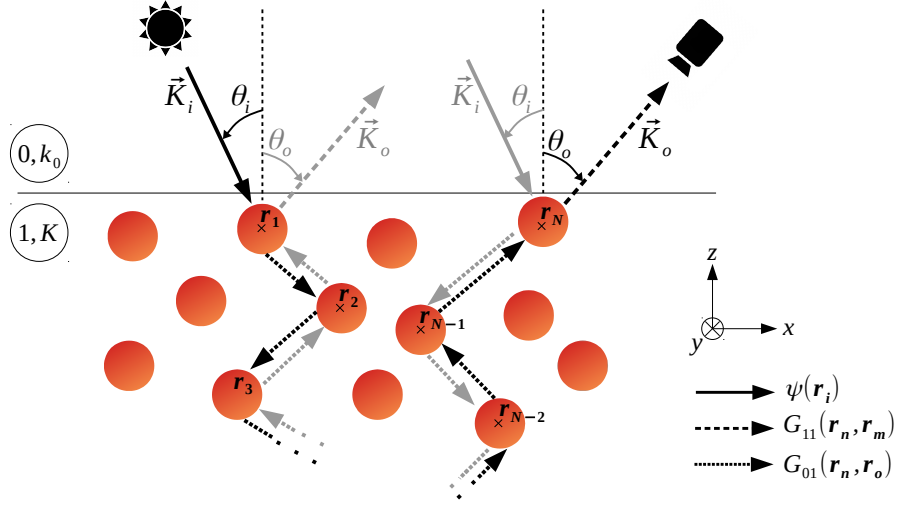


Fig. 1. N -th order multiple scattering in a medium composed of particles. The incident ray follows a path going from the particle at \mathbf{r}_1 to the one at \mathbf{r}_N . Interferences occur with the ray from \mathbf{r}_N to \mathbf{r}_1 . The incoherent part of the resulting field (denoted as \mathcal{L}_N in Section 5.1) contributes to the ladder term while its coherent part (denoted as C_N in Section 5.1) accounts for the cyclical term.

3.2. Foldy's approximation

For a sufficiently small density of scatterers, the effective wavenumber K can be expressed using the Foldy's approximation [21]:

$$K \approx k_0 + i \frac{2\pi N}{k_0} F \quad (1)$$

where F is the complex scattering amplitude, describing the scattering properties of the particles.

3.3. Light propagation

The propagation of light inside a medium containing scattering particles is illustrated by the Figure 1. The light ray coming from region 0 without being scattered is described by the incident field :

$$\psi_m(\mathbf{r}_i) = \exp(i\mathbf{K}_i \cdot \mathbf{r}_i) \quad (2)$$

where \mathbf{K}_i is of magnitude K given by the Foldy's approximation, and oriented in the incident direction.

After it has been scattered by a particle, light travels in the region 1 towards another scatterer, as if it was in a space free of scatterer. Under this hypothesis, the propagation of light from a position \mathbf{r}' towards \mathbf{r} is given by the Green's function $G(\mathbf{r}, \mathbf{r}')$, that satisfies the Helmholtz equation :

$$(\Delta + k^2)G(\mathbf{r}, \mathbf{r}') = \delta(\mathbf{r} - \mathbf{r}') \quad (3)$$

By averaging over the particles, the mean Green's function referring to the propagation of light from an inclusion to another is given as follows:

$$G_{11}(\mathbf{r}_n, \mathbf{r}_m) = \frac{\exp(i\mathbf{K} \cdot |\mathbf{r}_n - \mathbf{r}_m|)}{4\pi|\mathbf{r}_n - \mathbf{r}_m|} \quad (4)$$

153 where \mathbf{r}_m and \mathbf{r}_n are the positions of two distinct scatterers in the medium 1. In the same way,

$$G_{01}(\mathbf{r}_n, \mathbf{r}_o) = \frac{\exp(ik_0 r_o)}{4\pi r_o} \exp(-i\mathbf{K}_o \cdot \mathbf{r}_n) \quad (5)$$

154 describes the propagation from a scatterer at position \mathbf{r}_n in region 1 towards the camera at \mathbf{r}_o in
155 region 0. The vector \mathbf{K}_o is of magnitude K and oriented towards the camera.

156 3.4. Light scattering by one particle

157 The scattering events caused by the encountering of light with the n -th scatterer is described
158 using the transition operator T_n that we introduced as :

$$T_n(\mathbf{r}_n) = 4\pi F(\Theta_n) \delta(r_{in} - r_{on}) = 4\pi F(\Theta_n) \quad (6)$$

159 where $\Theta_n = \theta_{on} - \theta_{in}$ is the scattering angle between the incident direction on the n -th scatterer
160 θ_{in} and the outgoing direction θ_{on} .

161 The complex scattering amplitude $F(\Theta_n)$ is linked to the scattering phase function using the
162 relationship:

$$\rho p(\Theta_n) = \frac{4\pi N}{\kappa} |F(\Theta_n)|^2 \quad (7)$$

163 where ρ is the single scattering albedo and κ the extinction rate.

164 3.5. Enhanced back-scattering

165 The EBS theory offers a physical description of the back scattering phenomenon observed
166 in quite dense media. It is an extension of radiative transfer (RT) theory [19], [20]: the
167 so called *ladder terms* accounting for both single scattering $BRDF_{ebs, \mathcal{L}_1}$ and some multiple
168 scattering $BRDF_{ebs, \mathcal{L}_{2+}}$ takes into account the contribution of uncorrelated scattered fields
169 already described by the RT theory. This model also accounts for coherent scattered fields
170 that induce interference effects as light undergoes multiple scattering events in the medium. It
171 is described by a *cyclical term* $BRDF_{ebs, C}$ and results in a sharp peak in the back-scattering
172 direction.

173 The BRDF is then composed of three contributions:

$$BRDF_{ebs} = BRDF_{ebs, \mathcal{L}_1} + BRDF_{ebs, \mathcal{L}_{2+}} + BRDF_{ebs, C} \quad (8)$$

174 This model has been developed for thick layers of a medium composed of isotropic spherical
175 scatterers of radius r with a constant phase function $p(\Theta) = p$ embedded in a host medium
176 [17, 18, 22, 23].

177 Analytical expressions of the multiple scattering terms are obtained by considering that for
178 optically thick media with high albedo the resulting overall scattering statistically tends to be
179 isotropic. This is known as the *diffusion approximation* and leads to results in Eqs. 9.

$$\left\{ \begin{array}{l} BRDF_{ebs, \mathcal{L}_1} = \frac{\rho p(\Theta)}{\mu_o + \mu_i} \left[1 - \exp \left(-\kappa d \left(\frac{1}{\mu_o} + \frac{1}{\mu_i} \right) \right) \right] \end{array} \right. \quad (9a)$$

$$\left\{ \begin{array}{l} BRDF_{ebs, \mathcal{L}_{2+}} = \frac{3\rho^2}{1 - \mu_i^2 c^2} \left[\frac{2Q}{1 - \mu_o c} - \frac{\mu_i^2}{\mu_i + \mu_o} \right] \end{array} \right. \quad (9b)$$

$$\left\{ \begin{array}{l} BRDF_{ebs, C} = \frac{3\rho^2 [c + v(1 - \exp(-2c\tau_o))]}{2\mu_i \mu_o c v [(c + v)^2 + u^2]} \end{array} \right. \quad (9c)$$

The parameters u , v , c and Q in Eqs. 9 vary with the isotropy of the scatterers and with the geometry under which the medium is illuminated and observed. It has been described by [18] for

isotropic scatterers such as:

$$\left\{ \begin{array}{l} u = \frac{k_0}{\kappa} (\mu_i - \mu_o) \\ v = \frac{1}{2} \left(\frac{1}{\mu_i} + \frac{1}{\mu_o} \right) \\ \alpha = \frac{k_0}{\kappa} f \\ \kappa_{tr} = 1 - \rho \\ c = \sqrt{3(1 - \rho)\kappa_{tr} + \alpha^2} \\ Q = \frac{[1 + \mu_i c - (1 - \mu_i c)\exp(-2c\tau_o)]}{4c} \end{array} \right. \quad \begin{array}{l} (10a) \\ (10b) \\ (10c) \\ (10d) \\ (10e) \\ (10f) \end{array}$$

where f is the norm of the vector \mathbf{f} defined as difference between the projections of the normalized incoming and outgoing direction vectors (Figure 2) which allows the BRDF modelization in any azimuthal plane.

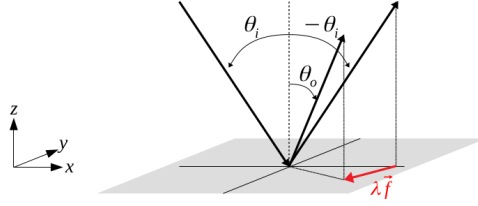


Fig. 2. Definition of the vector \mathbf{f} .

Only the single scattering term involves the phase function in such a case. [17] introduce the consideration of anisotropic scatterers but only with normal incidence. We will discuss the extension of the model for anisotropic scattering in the Section 5.

The last parameter involved in the BRDF expressions (Eqs. 9) is the extinction ratio τ_o that is defined as intrinsic to the scatterers' material. It accounts for internal reflections that may occur between the interface of the medium. A definition is given by [24]:

$$\tau_o = \frac{2}{3} \frac{1 - \bar{R}}{1 + \bar{R}} \quad (11)$$

$$\text{with } \bar{R} = \frac{3C_2 + 2C_1}{3C_2 - 2C_1 + 2} \quad \text{and} \quad C_i = \int_0^{\pi/2} R(\theta) \cos^i \theta \sin \theta d\theta$$

In the previous equations, $R(\theta)$ is the Fresnel's angular reflection coefficient [25]. The parameter τ_o thereby depends on the optical constants of the material the particles are made of and on the wavelength.

4. Sample description and BRDF measurements

The physical phenomena at stake in the appearance of a material can be inferred through the BRDF measurement.

4.1. Sample description

For the study of dry powder appearance we focused on synthetic nano-crystallized hematite $\alpha - \text{Fe}_2\text{O}_3$ powders with various colors, that we obtained using different routes allowing to control the nucleation and growth of $\alpha - \text{Fe}_2\text{O}_3$ crystallites in solution. These samples are presented on Figure 3

The samples we have denoted from 1 to 5 have been prepared following methods described by [26]. 1, 2 and 5 have been obtained by forced hydrolysis of Fe^{III} salts solutions in acidic conditions, while 3 and 4 are the results of the transformation of a ferrihydrite precipitate in aqueous suspension under basic conditions. We generated peanuts-like hematite particles 6 following the routes proposed by [27], NaH_2PO_4 salts. Sample 7 is a commercial Iron(III) oxide powder sample purchased from Puratronic®.

The color and the morphometry of each sample are respectively deduced from naked eye observations completed with optical microscopy using a Nikon Eclipse LV100ND microscope, and by scanning electron microscopy observations performed with a Zeiss Ultra+ microscope. Various grains' shape and size ranging from 10 nm to 10 μm are obtained. The small grains are characterized by a lighter red color (samples 1 to 5) while a darker purple hue is observed for the pigments with larger grains (samples 6 and 7). We may also note that samples 5, 6 and 7 can be described by two grain sizes: either two different size populations (sample 5), either large grains that are agglomerates of smaller ones (samples 6 and 7).

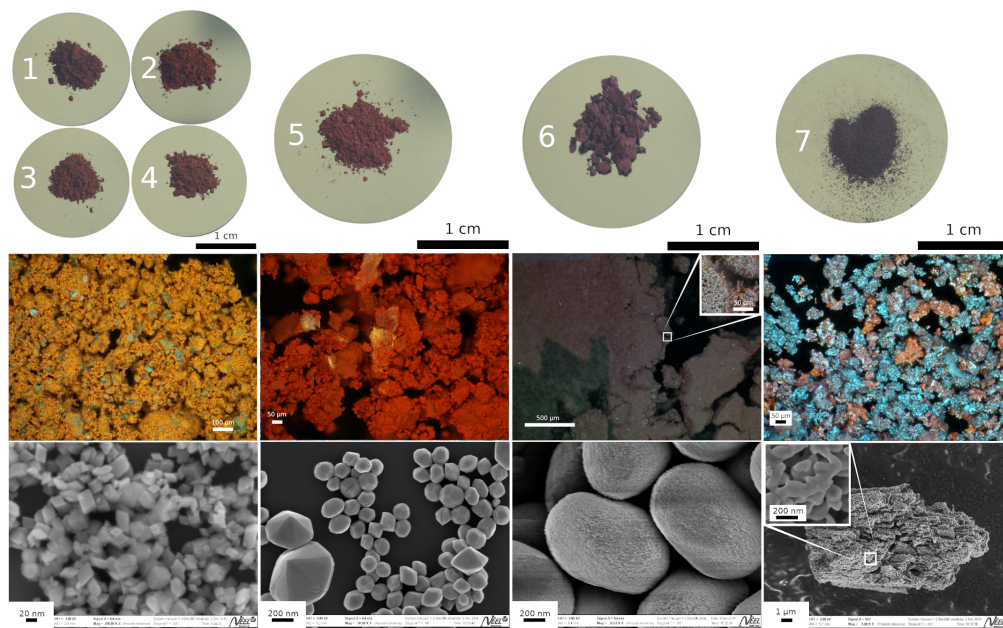


Fig. 3. $\alpha - \text{Fe}_2\text{O}_3$ hematite samples under study, showing various colors and grains' morphology. Upper row: The photographs are calibrated using an X-rite 24 patches Classic Colorchecker. Middle row: Observations using optical microscopy. Lower row: Samples' morphology observations using Scanning Electron Microscopy. The samples 1 to 4 show similar grain shape, with slightly different sizes from 10 to 50 nm in diameter, and light red hue. Sample 5 presents two size populations and shows a red-pinkish hue. Samples 6 and 7 have a more complex morphology with grains that seem to be agglomerations of smaller ones. The grains are larger and a darker purple hue is observed. According to optical microscopy, 7 is even composed of different types of grains, with different colors.

215 4.2. BRDF measurements

216 The whole BRDF of each sample is measured by combining two distinct measurements, depending
 217 on which scattering geometry is at stake. The first one does not account for the back-scattering,
 218 while the second one is specifically performed to account for this contribution.

219 4.2.1. Out the back-scattering

220 The main part of the BRDF is measured using the SHADOWS instrument [28], over 180 geometries:
 221 the scattered light is observed for $\theta_o \in [-70^\circ, 70^\circ]$, for incidences $\theta_i \in \llbracket 0^\circ, 20^\circ, 40^\circ, 60^\circ \rrbracket$
 222 and azimuthal angles $\varphi \in \llbracket 0^\circ, 30^\circ, 60^\circ, 90^\circ \rrbracket$, and 135° . The spectral range has been limited
 223 to 360 nm - 860 nm with a step of 20 nm. The reflectance measurements are calibrated with a
 224 Spectralon. Every point is measured with an integration time of 300 ms and averaged over 10
 225 spectra. Such measurement takes about 18 hours.

226 When it comes to a geometry where incident and observation directions are identical, the
 227 instrument's design causes the sensor to be obstructed by the light source. A specific device
 228 needs to be designed to evaluate the amount of light scattered in these directions.

229 4.2.2. In the back-scattering direction using an in-house-built set-up

230 Our design for measuring the back-scattering contribution to the BRDF is inspired from the
 231 work of [29] and [8]. As these only deal with vertically held samples, they cannot be used for
 232 studying dry powders. We propose a new design to allow the measurement of any horizontally
 233 held sample.

234 We chose an halogen light source to normally illuminate the sample after being reflected by a
 235 beam splitter at 45° . The size of the illumination spot is minimized by focusing the light with a
 236 50 mm focal lens. An additional diaphragm is added to clean the focused beam. The direction of
 237 the incident light θ_i is adjusted by positioning the beam splitter at an angle of $45^\circ + \theta_i/2$. As the
 238 light interacts with the powder, it is scattered in every directions and preferably back into the
 239 incident direction. It is then partially transmitted through the beam splitter and collected by a
 240 Thorlabs F950FC-A collimator. The latter is fixed on a vertical rotating plate so that we can scan
 241 different observation directions around the exact back-scattering one in the incident plane. We
 242 use a fiber spectrometer OceanOptics USB650 along with the SpectraSuite software in order to
 243 detect and visualize the measured signal.

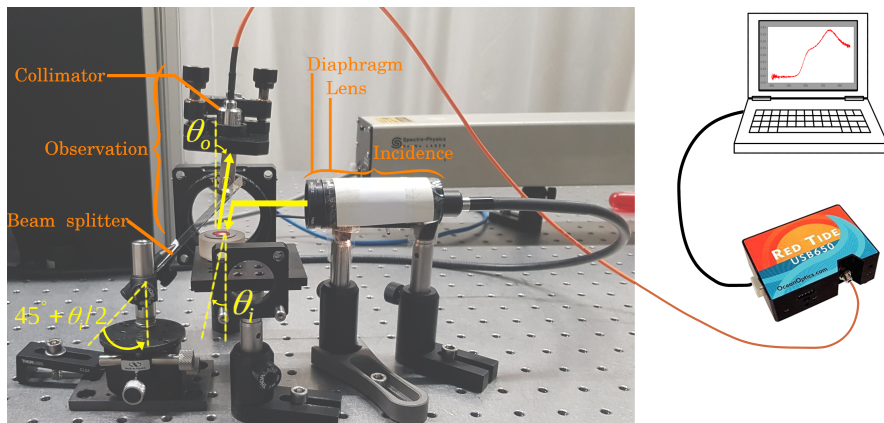


Fig. 4. Back-scattering measurement device. The beam of a white source is focused on the sample's surface at an incidence θ_i using a 50 mm focal lens and a beam splitter. The reflected light is collected through a collimator in different observation directions θ_o .

244 In the incident plane ($\varphi = 0^\circ$), we scan the observation angles in the range $[\theta_i - 10^\circ, \theta_i + 10^\circ]$
 245 with a step of 2° , for incidences $0^\circ, 20^\circ$ and 40° . The reflectance measurements are calibrated with
 246 a Spectralon. The integration time is chosen to maximize the detected signal and an averaging
 247 over 5 spectra is performed to minimize the noise. Less than 20 seconds is necessary to measure
 248 one spectrum.

249 4.2.3. Complete measurement

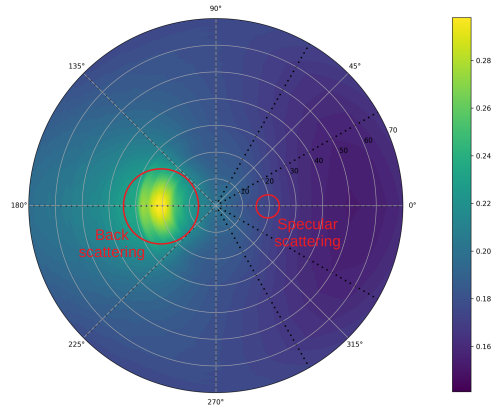


Fig. 5. Complete BRDF of the hematite powder sample 1 at the wavelength 700 nm for an incidence $\theta_i = 40^\circ$. The measured geometries are spotted with black dots, and the intermediate values are interpolated. Light is mostly reflected in the backward direction, and a very weak specular scattering peak may be observed as well. The spreading of the back scattering peak with the azimuth angle is due to the colormap interpolation between the measured points.

250 As the two measurements are performed independently, they happen to be shifted in amplitude
 251 from one another. This may be caused by the underestimation of the back scattering of the
 252 spectralon used for photometric calibration. Since the difference is smaller than 5%, a re-scaling
 253 of the back-scattering measurement is done so it matches the goniometer results.

254 A typical experimental BRDF is shown figure 6 after merging the measured data. The
 255 measurements show that the BRDF of dry hematite powders is composed of an overall diffuse
 256 contribution, and two directional scattering phenomena including mainly back-scattering and
 257 some specular scattering (Figure 5). The BRDFs of characterized samples vary in intensity and
 258 width of the specularly and back scattered lobes. We give results for the six other samples under
 259 study in Supplementary Work.

260 5. Powder BRDF Model

261 As shown by the measurements on Figure 5, powders' BRDF mainly involves back-scattering
 262 and almost no specular scattering which makes the usual specular BRDF models ineffective to
 263 reproduce their appearance.

264 Although our model is derived from a study on pure nano-crystallized hematite powders, we
 265 chose a physically-based approach so that it can be applied to any other pigment. It involves
 266 both chemical composition and morphological parameters to accurately account for the color
 267 variations observed on such pigments. Moreover it allows to consider either isotropic or
 268 anisotropic scatterers. Inspired by both RTLSR and Spectralon's models, our model is divided

269 into two contributions respectively accounting for volume and surface scattering.

$$BRDF = A_v BRDF_v + A_s BRDF_s \quad (12)$$

270 These two contributions are weighted with the amplitude parameters A_v and A_s .
 271 The main difference with the previously introduced models is that, based on the EBS theory the
 272 back scattering is considered as part of the volume contribution. The surface contribution is then
 273 reduced to specular scattering caused by surface roughness.

274 5.1. Volume scattering

275 As EBS theory is established within the diffusion approximation, the averaged scattering is
 276 assumed to be isotropic. This greatly simplifies the multiple scattering contribution by considering
 277 the scattering phase function as constant over the whole scattering hemisphere. The anisotropic
 278 scattering of each particle is accounted for by choosing the phase function parameter g involved
 279 in the single scattering contribution. The extension of the model for taking into account this
 280 anisotropy in multiple scattering has only been done for a normal incidence by Tsang et al. [17].

281 In the following we expose the calculations that we made in order to consider anisotropic
 282 scattering in both single and multiple scattering terms for any $\theta_i/(\theta_o, \varphi_o)$ geometry. The final
 283 model only involves two variable parameters (g, κ) that rely on the physical and chemical
 284 properties of the material that is under study.

285 **First order ladder term \mathcal{L}_1 :** This contribution accounts for light that is only scattered once
 286 before being observed and is similar to the one introduced in Section 3.5. The anisotropy is taking
 287 care of by the scattering phase function involved in the analytical expression of $BRDF_{EBS, \mathcal{L}_1}$ in
 288 Eq. 9.

289 **Multiple ladder term \mathcal{L}_{2+} :** The phase function is involved at every scattering event that
 290 light encounters as it travels the particulate medium. We denote P_i and P_o respectively the first
 291 and the last particles that are responsible for light scattering along a light path.

292 At the second scattering order, the light is first incoming on P_i , scattered with an angle Θ_i
 293 towards the particle P_o , and finally scattered towards the observer with an angle Θ_o as illustrated
 294 by the Figure 6.

295 For the n -th scattering order, light undergoes n scattering events. As for the second order, it
 296 undergoes a first one described by the angle Θ_i while encountering the particle P_i and last one
 297 with the particle P_o and the angle Θ_o . But it also interacts with $n - 2$ other particles in between,
 298 resulting in $n - 2$ scattering events respectively described by the scattering angles $\Theta_k = \theta_{ik} - \theta_{ok}$,
 299 difference between the incoming direction θ_{ik} and outgoing direction θ_{ok} on the k -th particle,
 300 with $k = \llbracket 2 ; \infty \rrbracket$ as it is shown on the Figure 6.

301

By averaging over all the possible paths that light can follow inside the medium while
 encountering n scatterers, we can write the n -th order ladder term as follows:

$$\begin{aligned} \mathcal{L}_n = & \frac{(4\pi)^{n-2}(\rho\kappa)^n}{r^2} \\ & \times \int |p(\Theta_n)|^2 |G_{11}(\mathbf{r}_n, \mathbf{r}_{n-1})|^2 \dots |G_{11}(\mathbf{r}_2, \mathbf{r}_1)|^2 |p(\Theta_1)|^2 \exp\left(\kappa\left(\frac{z_1}{\mu_o} + \frac{z_n}{\mu_i}\right)\right) d\mathbf{r}_1 \dots d\mathbf{r}_n \end{aligned} \quad (13)$$

302 with r the distance from the sample to the observation point.

303 The total ladder term accounting for multiple scattering can be written in a recursive way,
 304 giving:

$$\mathcal{L}_{2+} = \int \int \exp\left(\kappa\left(\frac{z_i}{\mu_o} + \frac{z_o}{\mu_i}\right)\right) A(\mathbf{r}_i, \mathbf{r}_o) d\mathbf{r}_i d\mathbf{r}_o \quad (14)$$

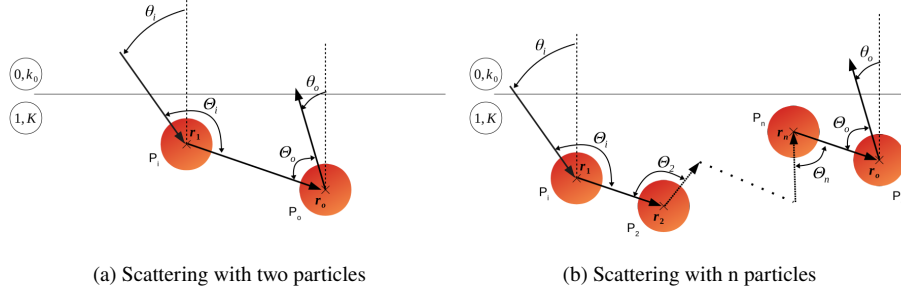


Fig. 6. Multiple scattering with two and n particles. The first scatterer that light encounters as it travels inside the medium is denoted as P_i and involves a scattering event described by the angle θ_i . The last scattering event before light goes out of the medium is caused by the scatterer P_o with an angle θ_o . In between these two scatterers, light is scattered with an angle θ_k at each interaction with a particle k .

305 with $A(\mathbf{r}_i, \mathbf{r}_o)$ defined such as:

$$A(\mathbf{r}_i, \mathbf{r}_o) = \left(\frac{\rho\kappa}{4\pi}\right)^2 p(\theta_1)p(\theta_o) \frac{\exp(\kappa|\mathbf{r}_i - \mathbf{r}_o|)}{|\mathbf{r}_i - \mathbf{r}_o|^2} + \int \left(\frac{\rho\kappa}{4\pi}\right) p(\theta_n) \frac{\exp(\kappa|\mathbf{r}_i - \mathbf{r}_n|)}{|\mathbf{r}_i - \mathbf{r}_n|^2} A(\mathbf{r}_n, \mathbf{r}_o) d\mathbf{r}_n \quad (15)$$

306 Note that contrary to the ladder term defined by the Eq. 9, our model involves a varying
 307 scattering phase function whose expression is chosen to better model the material under study. If
 308 one wants to describe isotropic scattering a constant phase function such as $p(\theta) = p$ should be
 309 used which leads back to the expression originally introduced in Section 3.5.

310

311 The resulting BRDF of the ladder contribution is then given by:

$$BRDF_{\mathcal{L}_{2+}} = \frac{4\pi r^2 \mathcal{L}_{2+}}{a\mu_i\mu_o} \quad (16)$$

312 where a is the area of the sample under studied.

313 **Multiple cyclical scattering C :** As for the ladder term, we are aiming to take into account
 314 the anisotropic scattering of particles in the cyclical term. We will use the same assumptions as
 315 illustrated by the Figure 6. We consider a ray of light that is scattered by n particles as it follows
 316 a path inside the medium. By accounting for the correlation between this path and its reversal
 317 and averaging over all the possible paths, the n -th order cyclical term can be written:

$$C_n = \frac{(4\pi)^{n-2}(\rho\kappa)^n}{r^2} \int |p(\theta_n)|^2 |G_{11}(\mathbf{r}_n, \mathbf{r}_{n-1})|^2 \dots |G_{11}(\mathbf{r}_2, \mathbf{r}_1)|^2 |p(\theta_1)|^2 \\ \times \cos\left(k(\mu_i - \mu_o)(z_1 - z_n)\right) \exp\left(\frac{\kappa}{2}\left(\frac{1}{\mu_o} + \frac{1}{\mu_i}\right)(z_1 + z_n)\right) d\mathbf{r}_1 \dots d\mathbf{r}_n \quad (17)$$

318 The complete cyclical contribution is obtained by summing over the n -th orders and can be
 319 simplified replacing G_{11} by its definition (Eqs. 4). By using the new expression of $A(\mathbf{r}_i, \mathbf{r}_o)$
 320 given by Eq. 15:

$$C = \int \int \cos(2k(\mu_i - \mu_o)(z_o - z_i)) \exp\left(\frac{\kappa}{2}\left(\frac{z_i}{\mu_o} + \frac{z_o}{\mu_i}\right)\right) A(\mathbf{r}_i, \mathbf{r}_o) d\mathbf{r}_i d\mathbf{r}_o \quad (18)$$

Once again, the scattering properties of each particle that plays a role in the n -th order scattering is explicitly involved through the varying phase function. The use of a constant phase function $p(\theta) = p$ brings back to the isotropic case already discussed in Section 3.5.

Finally, the cyclical term contributes to the complete appearance of the dry powder through the partial BRDF:

$$BRDF_C = \frac{4\pi r^2 C}{a\mu_i\mu_o} \quad (19)$$

Under the *Diffusion approximation*, the multiple scattering terms 16 and 19 are reduced to the analytical formulas given by the Eqs. 9. By extending the work from [17] the parameters involved in the model are defined such as in Eqs. 10 so that the model is valid for any geometry including various incident directions, but using $\kappa_{tr} = 1 - \rho g$ to also account for the phase function anisotropy in the multiple scattering.

5.2. Surface scattering

In our model, surface scattering is reduced to the specular contribution. The light that is incoming on a rough surface such as the interface between air and a dry powder is scattered in a lobe around the specular direction.

Two options have been considered to include such a phenomenon in our model. The former is to model the specular peak by a gaussian function. According to the measurements performed in Section 4 the specular scattering is very weak so this simple method is reliable enough to reproduce the specular contribution of dry powders, although it is empirical. By assuming a uniform distribution of the surface normals, it requires only one parameter which is the gaussian half width σ . With this modeling the surface scattering BRDF is written as:

$$BRDF_s = \frac{1}{\sigma\sqrt{2\pi}} \exp\left(\frac{-\theta^2}{2\sigma^2}\right) \quad (20)$$

The second option, which is the one we chose to use, relies on the physical approach from Harvey-Shack [6] that accounts for diffraction effects caused by the surface asperities. Using this theory, the incoming light on a rough surface is then scattered around the specular direction according to the following BRDF:

$$BRDF_s = \frac{4\pi^2}{\lambda^4} (\cos \theta_i + \cos \theta_o)^2 PSD(\mathbf{f}) \quad (21)$$

where the power spread function (PSD) models a rough surface topography. We chose a gaussian power spread function, involving a roughness parameter σ_s and a correlation length l_c that quantifies the mean distance for which the surface roughness of two points on the surface are completely independent.

$$PSD(\mathbf{f}) = \pi\sigma_s^2 l_c^2 \exp(-\pi^2 l_c^2 (f_x^2 + f_y^2)) \quad (22)$$

5.3. Complete model

Our complete model is the weighted sum of volume and surface contributions according to Eq. 12 respectively given by the adapted enhanced back scattering model and a specular model. Note that the roughness parameter involved in the surface contribution has been included in the amplitude parameter $A'_s = A_s \sigma_s^2$ in order to reduce the number of optimization parameters.

$$BRDF = A_v [BRDF_{\mathcal{L}_1}(g) + BRDF_{\mathcal{L}_{2+}}(g) + BRDF_C(g, \kappa)] + A'_s BRDF_s(l_c) \quad (23)$$

355 The model depends on a total of 5 empirical and physical parameters to accurately simulate
 356 the BRDF of dry powder. As it is shown in the Section 6, our model works even better while
 357 including another physical parameter to refine which is the *effective radius* of the grains, defined
 358 as the mean size of the grains actually seen by the incoming light and therefore responsible for
 359 the scattering. The influence of such parameter is shown on Figure 7. The parameters involved
 in our model are summarized in Table 1.

Volume scattering	
A_v	Intensity of volume scattering
g	Scattering anisotropy
κ	Extinction rate
r	effective radius (optional)
Surface scattering	
A'_s	Intensity of surface scattering
l_c	Correlation length

Table 1. Parameters involved in our BRDF model. The model can be optimized by refining only 5 parameters while the grain radius r is fixed, or by refining 6 parameters including the same 5 previous ones and an effective radius.

360

361 6. Results

362 In order to check on the ability of the model to simulate the pigments' BRDF, we applied it to
 363 the hematite powders measurements by optimizing the variable parameters of Table 1. We used
 364 the least squares method to fit the measurement data. A first option is to optimize while using a
 365 fixed radius. The average dimensions of the grains of a sample is deduced from SEM images and
 366 reduced to only one dimensional parameter by computing the radius of a sphere that is equivalent
 367 to the grain. To better account for the shape anisotropy this radius is computed so that the ratio of
 368 the surface over the volume of the equivalent sphere and of the grain remains constant. The final
 369 mean radius is obtained by averaging on the radii of multiple grains that are in the field of view
 370 of a single SEM image. However, in the following we chose to optimize on the grains' effective
 371 radius as it leads to better results. Indeed it allows a nicer modeling of the back scattering peak
 372 amplitude, while keeping values pretty close to the radius deduced from microscopy observations
 373 (see Table 2). The comparison of the two optimizations performed on sample 2 is shown on
 374 Figure 7. The optimization is performed for all geometries of incidence whose back scattering
 375 contribution has been measured, which corresponds to incidence smaller than 60° . We only
 376 account for the measurements at the wavelength 700nm, the spectral dependency of the model
 377 being discuss later on.

378 For comparison, the same optimization process is performed using both Spectralon and RTLSR
 379 models adapted to be relevant in the case of dry powders. Such adaptations to the original models
 380 are detailed in Supplemental work. Results of the optimization process for the sample 1 are given
 381 on the Figures 8, 9, and 10. The results obtained for other samples are listed in Supplementary
 382 work.

383

384 Our model is able to reproduce the measured BRDF of hematite powders with an accuracy
 385 comparable to that of the Spectralon mode ($< 8\%$ of the reflectance factor), but with a much lower

complexity: only 6 parameters related to physical properties of the samples are required against 12 empirical ones for the Spectralon's model. It is particularly efficient in the case of samples whose morphology is easily characterized, that is to say for the samples with well-crystallized single-crystals. Both the back-scattering and the specular contributions are detected and modeled, even though the latter is sometimes too weak for the modeling to be reliable. Errors are mostly spotted around the back scattering peak because of the measurements' poor sampling and interpolation at these geometries. Let's note that we have encountered difficulties in the modelization of samples 3 and C's BRDFs that we attributed to the more complex morphology of these powders. These powders are not monodisperse since they show two size populations and agglomerations of grains. An extension of our model is proposed in supplementary work to deal with powders presenting two grain size populations.

Sample	Radius SEM (nm)	Effective radius (nm)		
1	13 ± 3.0	17		
2	12 ± 1.6	16		
3	22 ± 3.7	16		
4	25 ± 4.1	15		
Sample	Large radius SEM (nm)	Effective radius (nm)	Small radius SEM (nm)	Effective radius (nm)
5	83 ± 34	83	47 ± 5.3	46
6	687 ± 64.0	687	10 ± 0.4	43
7	2222 ± 1054	2222	49 ± 13	49

Table 2. Comparison of the radius deduced from SEM observations and the effective radius obtained by the optimization of our model. For samples 5 to 7, the model extension for two size populations presented in Supplementary work is used. As it takes two different radii to optimize, two effective radii are obtained.

Since the refined parameters permit our model to quite precisely fit with the measurements in any geometry, it appears that none of them depends on the incoming, outgoing and azimuthal directions. The model is then able to predict the appearance of the studied powder in any other geometry that hasn't been considered during its optimization. The results are convenient even for more grazing angles such as incidence $\theta_i = 60^\circ$ as shown on Figure 7.

7. Discussion & Conclusion

From BRDF measurements, we highlighted that in the particular case of dry powders the light is mainly back scattered. We proposed a new BRDF model accounting for three different scattering interactions: single scattering, incoherent multiple scattering and coherent multiple scattering responsible for the sharp peak in the backward direction. It is a semi-empirical and analytical model based on the propagation of light inside a granular medium that involves the physico-chemical properties of the powders connected only six refinement parameters.

The model has been validated against the BRDF measurements of seven $\alpha - \text{Fe}_2\text{O}_3$ hematite powders, and compared to two adapted existing models. Ours is able to reproduce the measured BRDF with an accuracy comparable to the one of the Spectralon's model, but with a much lower complexity. It can be used in its original form to reproduce the appearance of a mono

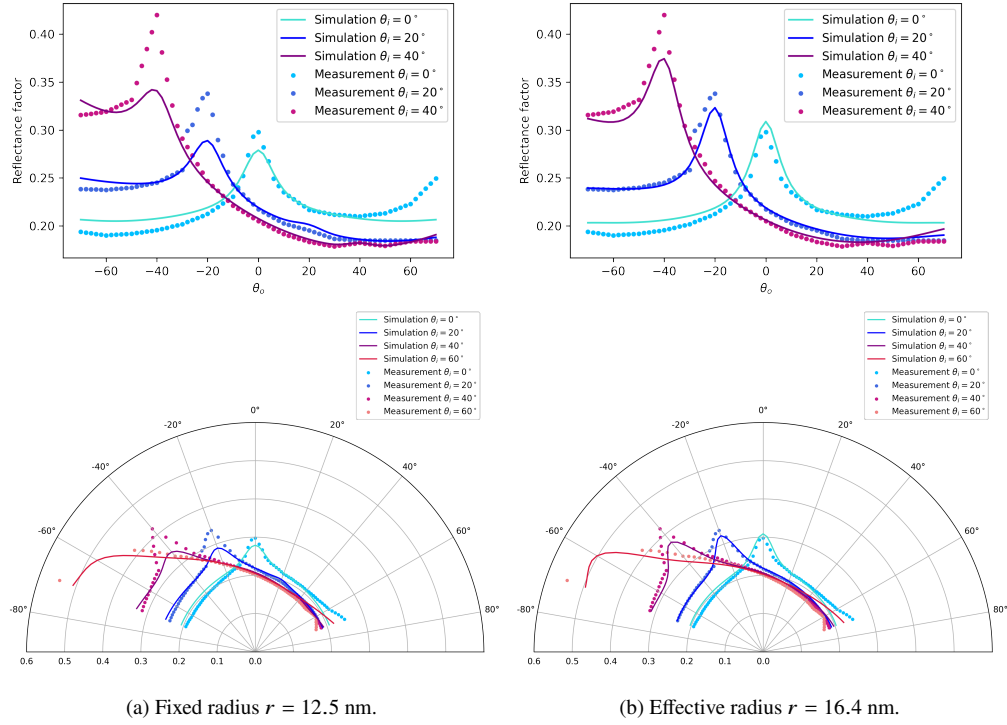


Fig. 7. Influence of the grain radius optimization on the results of sample 2, in the incident plane ($\varphi = 0^\circ$) for incidences $\theta_i = 0^\circ$, 20° and 40° . The effective radius found by optimization ($r = 16.4$ nm) is pretty close to the theoretical result deduced from SEM observations ($r = 12.5$ nm). On the polar representation, the prediction of our model for incidence $\theta_i = 60^\circ$ is also given.

413 disperse powder with spherical grains, or in its extended form presented in Supplementary work
 414 to account for more complex morphology involving multiple grains size populations.

415

416 Our model still has some limitations. The results obtained for specular scattering are quite
 417 questionable since the specular contribution is very weak and almost unnoticeable on the BRDF
 418 measurements. A more accurate model should be established by studying powders showing shiny
 419 and sparkling reflections such as eye shadow.

420

421 More generally, the model is not able to predict the appearance of any powder whose BRDF
 422 has not been measured beforehand. This would require to establish a relationship between the
 423 variable parameters of the model and the physico-chemical parameters of the material the powder
 is composed of, which requires to study much more samples with more variability in sizes.

424

425 The validity of the model's wavelength dependency is also a main issue that couldn't be
 426 solved throughout this work. At smaller wavelengths, the optimization is not robust enough to
 427 lead to nice fitting results (see Figure 11). This might be caused by a poor knowledge of the
 428 optical constants of the studied material which is the only fixed parameter known as spectrally
 429 varying. Indeed, it is mainly described by the optical constant at stake whose value appears to be
 430 quite doubtful according to the discrepancies between the results in the literature [30, 31]. Such
 431 uncertainties are often ignored in both material science and computer graphics whereas it surely
 affects the results.

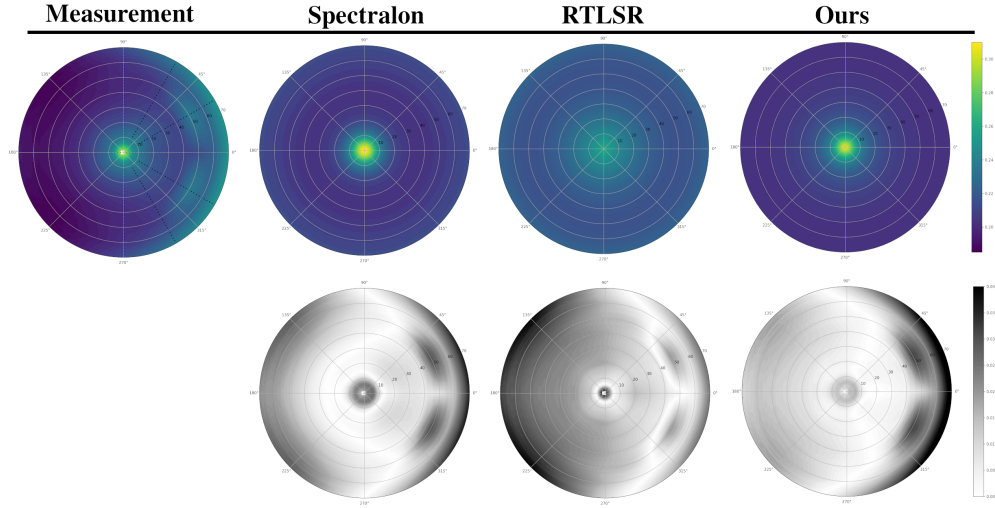


Fig. 8. Upper row: Simulation of sample 1's BRDF using our model, spectralon and RTLSR models adapted to dry powders, at incidence $\theta_i = 0^\circ$. Lower row: difference between the measurement and the simulation.

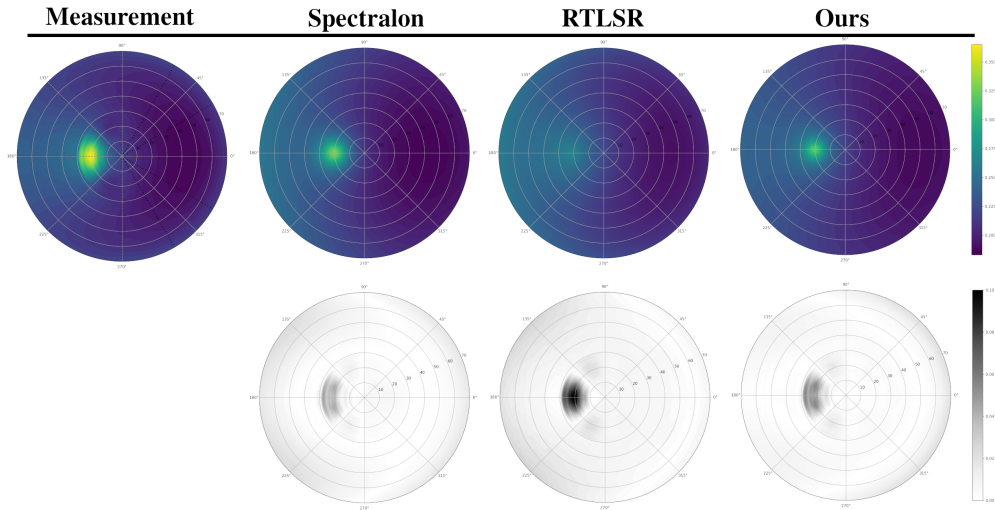


Fig. 9. Upper row: Simulation of sample 1's BRDF using our model, spectralon and RTLSR models adapted to dry powders, at incidence $\theta_i = 20^\circ$. Lower row: difference between the measurement and the simulation.

432

433 As a future work we would like to implement our dry powder BRDF model in a physically
 434 based renderer so that photo-realistic renderings of the powders can be made. This would first
 435 allow the validation of the model by comparing the rendered image with photographs of the actual
 436 samples. It would also permit, by letting the user choose the values of the variable parameters to
 437 either reproduce the appearance of other powder materials, or to create new ones.

438 Although the model has been tested for only one material, we believe it can be used for any
 439 other pure pigment. In the case of parietal paintings, ochers (mixture of one iron-based coloring

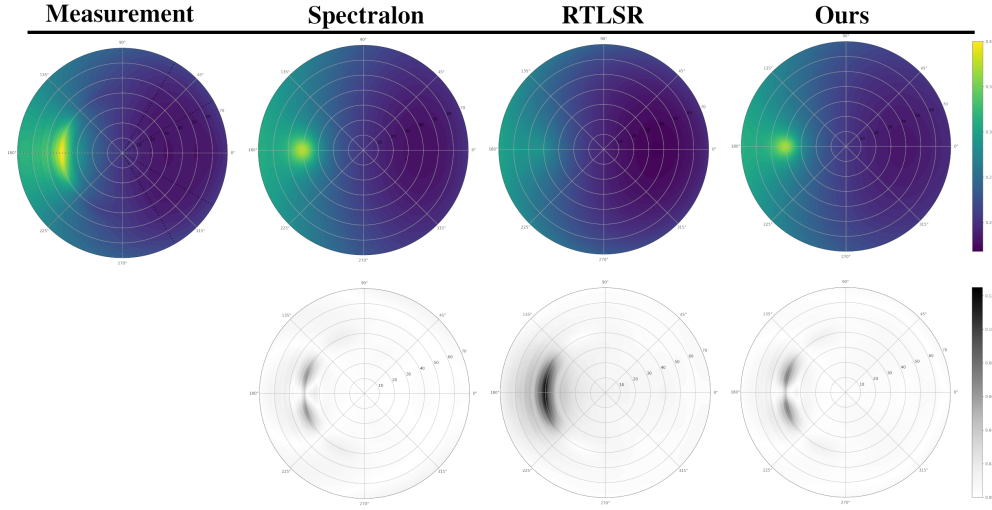


Fig. 10. Upper row: Simulation of sample 1's BRDF using our model, spectralon and RTLSR models adapted to dry powders, at incidence $\theta_i = 40^\circ$. Lower row: difference between the measurement and the simulation.

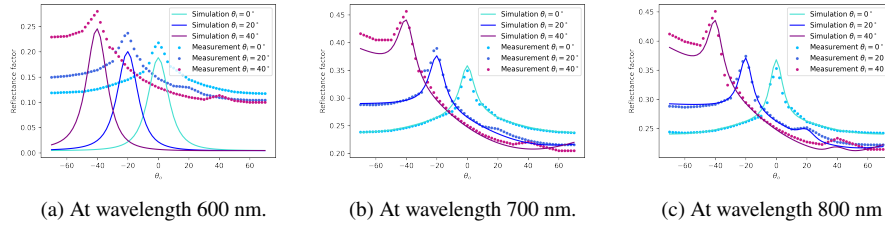


Fig. 11. Optimization of our model at different wavelengths using the optical constants from [30]. For smaller wavelengths, our model is not able to accurately fit the measurements.

440 pigment and colorless powders such as clays) and mixtures of different pigments were more
 441 commonly used than pure and almost pure iron oxide. In order to reproduce photo-realistic
 442 appearance of such paintings, we would like to extend our model to more complex powders.

443 The assumption of optically thick layer of powder is also too restrictive. An extension of the
 444 enhanced back scattering theory for thin films and isotropic scatterers has been proposed by [18]
 445 and may be a good starting point for our model adaptation, leading to a better reproduction of the
 446 appearance of painting layers.

447
 448 **Acknowledgments.** The authors would like to thank Alain Ibanez and Simon Giraud (Institut
 449 Néel) for the hematite samples syntheses. Our thanks also go to Corinne Félix (Institut Néel)
 450 for her help in developing the back-scattering measurement device, as well as Bernard Schmitt
 451 and Olivier Brissaud (IPAG) for their help in the reflectance measurements using SHADOWS
 452 gonio-spectro-photometer. This work was financially supported by the French National Research
 453 Agency in the framework of the Investissements d'Avenir program (ANR-15-IDEX-02, Cross
 454 Disciplinary Program Patrimoine).

456 **Supplemental document.** See Supplement 1 for supporting content.

457 **References**

- 458 1. E. Chalmin, M. Menu, M.-P. Pomiès, C. Vignaud, N. Aujoulat, and J.-M. Geneste, “Les blasons de lascaux,”
459 L’anthropologie **108**, 571–592 (2004).
- 460 2. M. Gerardin, N. Holzschuch, A. Ibanez, B. Schmitt, and P. Martinetto, “Influence of micro-structural features on
461 the colour of nanocrystallised powders of hematite and visible-nir reflectance spectra simulations,” J. international
462 colour association **26**, 41–48 (2021).
- 463 3. J. R. Frisvad, N. J. Christensen, and H. W. Jensen, “Computing the scattering properties of participating media using
464 lorenz-mie theory,” in *ACM SIGGRAPH 2007 papers*, (2007), pp. 60–es.
- 465 4. C. F. Bohren and D. R. Huffman, *Absorption and scattering of light by small particles* (John Wiley & Sons, 2008).
- 466 5. R. L. Cook and K. E. Torrance, “A reflectance model for computer graphics,” ACM Transactions on Graph. (ToG) **1**,
467 7–24 (1982).
- 468 6. A. Krywonos, “Predicting surface scatter using a linear systems formulation of non-paraxial scalar diffraction” (2006).
- 469 7. P. Beck, A. Pommerol, N. Thomas, B. Schmitt, F. Moynier, and J.-A. Barrat, “Photometry of meteorites,” Icarus **218**,
470 364–377 (2012).
- 471 8. M. Lévesque and M. Dissanka, “Measurement and modeling of the spectralon spectro-polarimetric bidirectional
472 reflectance distribution function (brdf)” (2016).
- 473 9. J.-L. Roujean, M. Leroy, and P.-Y. Deschamps, “A bidirectional reflectance model of the earth’s surface for the
474 correction of remote sensing data,” J. Geophys. Res. Atmospheres **97**, 20455–20468 (1992).
- 475 10. W. Lucht, C. B. Schaaf, and A. H. Strahler, “An algorithm for the retrieval of albedo from space using semiempirical
476 brdf models,” IEEE Transactions on Geosci. Remote. sensing **38**, 977–998 (2000).
- 477 11. J. Ross, “The radiation regime and architecture of plant stands. the hague: Dr. w,” Junk Publ. doi **10**, 978–94 (1981).
- 478 12. X. Li and A. H. Strahler, “Geometric-optical bidirectional reflectance modeling of a conifer forest canopy,” IEEE
479 Transactions on Geosci. Remote. Sens. pp. 906–919 (1986).
- 480 13. W. Wanner, X. Li, and A. Strahler, “On the derivation of kernels for kernel-driven models of bidirectional reflectance,”
481 J. Geophys. Res. Atmospheres **100**, 21077–21089 (1995).
- 482 14. Z. Jiao, A. Ding, A. Kokhanovsky, C. Schaaf, F.-M. Bréon, Y. Dong, Z. Wang, Y. Liu, X. Zhang, S. Yin *et al.*,
483 “Development of a snow kernel to better model the anisotropic reflectance of pure snow in a kernel-driven brdf model
484 framework,” Remote. sensing environment **221**, 198–209 (2019).
- 485 15. T. Nilson and A. Kuusk, “A reflectance model for the homogeneous plant canopy and its inversion,” Remote. Sens.
486 Environ. **27**, 157–167 (1989).
- 487 16. W. Ni, X. Li, C. E. Woodcock, M. R. Caetano, and A. H. Strahler, “An analytical hybrid gort model for bidirectional
488 reflectance over discontinuous plant canopies,” IEEE Transactions on Geosci. Remote. Sens. **37**, 987–999 (1999).
- 489 17. L. Tsang and J. A. Kong, *Scattering of electromagnetic waves: advanced topics*, vol. 26 (John Wiley & Sons, 2004).
- 490 18. M. B. Van Der Mark, M. P. van Albada, and A. Lagendijk, “Light scattering in strongly scattering media: multiple
491 scattering and weak localization,” Phys. Rev. B **37**, 3575 (1988).
- 492 19. S. Chandrasekhar, *Radiative transfer* (Courier Corporation, 2013).
- 493 20. A. Ishimaru, *Wave propagation and scattering in random media*, vol. 2 (Academic press New York, 1978).
- 494 21. L. L. Foldy, “The multiple scattering of waves. i. general theory of isotropic scattering by randomly distributed
495 scatterers,” Phys. review **67**, 107 (1945).
- 496 22. B. Bret, “Multiple light scattering in porous gallium phosphide,” Ph.D. thesis, Universiteit Twente (2005).
- 497 23. S. Lönn and D. Kroon, “Utilizing enhanced backscattering for determination of scattering properties in turbid media,”
498 Lund Reports At. Phys. (2011).
- 499 24. J. Zhu, D. Pine, and D. Weitz, “Internal reflection of diffusive light in random media,” Phys. Rev. A **44**, 3948 (1991).
- 500 25. M. Born and E. Wolf, *Principles of optics: electromagnetic theory of propagation, interference and diffraction of*
501 *light* (Elsevier, 2013).
- 502 26. U. Schwertmann and R. M. Cornell, *Iron oxides in the laboratory: preparation and characterization* (John Wiley &
503 Sons, 2008).
- 504 27. T. Sugimoto, A. Muramatsu, K. Sakata, and D. Shindo, “Characterization of hematite particles of different shapes,” J.
505 colloid interface science **158**, 420–428 (1993).
- 506 28. S. Potin, O. Brissaud, P. Beck, B. Schmitt, Y. Magnard, J.-J. Correia, P. Rabou, and L. Jocou, “Shadows: a
507 spectro-gonio radiometer for bidirectional reflectance studies of dark meteorites and terrestrial analogs: design,
508 calibrations, and performances on challenging surfaces,” Appl. optics **57**, 8279–8296 (2018).
- 509 29. L. Belcour, R. Pacanowski, M. Delahaie, A. Laville-Geay, and L. Eupherte, “Bidirectional reflectance distribution
510 function measurements and analysis of retroreflective materials,” JOSA A **31**, 2561–2572 (2014).
- 511 30. M. R. Querry, “Optical constants,” Tech. rep., Missouri Univ-Kansas City (1985).
- 512 31. A. H. M. J. Triaud, “Refractive indices of hematite,” [http://eodg.atm.ox.ac.uk/ARIA/data?](http://eodg.atm.ox.ac.uk/ARIA/data?Minerals/Hematite/(Triaud_2005)/hematite_Triaud_2005.ri)
513 [Minerals/Hematite/\(Triaud_2005\)/hematite_Triaud_2005.ri](http://eodg.atm.ox.ac.uk/ARIA/data?Minerals/Hematite/(Triaud_2005)/hematite_Triaud_2005.ri).